

RESEARCH ARTICLE

An investigation of atmospheric rivers impacting heavy rainfall events in the North-Central Mississippi River Valley

Jordan L. Rabinowitz¹ | Anthony R. Lupo^{1,2,3} | Patrick S. Market¹ | Patrick E. Guinan^{1,3}

¹Atmospheric Science Program, School of Natural Resources, University of Missouri, Columbia, Missouri

²Department of Natural Resources Management and Land Cadastre, Belgorod State University, Belgorod, Russia

³Missouri Climate Center, Waters Hall, University of Missouri, Columbia, Missouri

Correspondence

Jordan L. Rabinowitz, Atmospheric Science Program, School of Natural Resources, University of Missouri, 302 E ABNR Building, Columbia, MO 65211.

Email: jlrw6@mail.missouri.edu

Funding information

USDA, Grant/Award Numbers: 58-3622-4-025, 58-5070-5-018

During the latter part of the 20th century and into the 21st century, research has focused on evaluating how to more effectively utilize upper-air soundings and satellite analysis of atmospheric water vapour transport pathways typically referred to as “atmospheric rivers” (ARs) in order to better forecast heavy rainfall events. Rainfall associated with ARs may include a significant portion of monthly and seasonal rainfall when they occur within the North-Central Mississippi Valley Region. A comprehensive analysis of surface and upper-air maps and upper-air soundings and the associated vertical wind profiles is conducted to help build a relationship between the intensity and duration of heavy rainfall events during the period 2000–2015. The goal is to develop a proxy by which rainfall events can be predicted more accurately and work towards developing improved operational forecast protocols. In addition, a secondary goal is to evaluate possible connections between AR dynamics as highlighted using Hybrid Single-Particle Lagrangian Integrated Trajectory (HYSPLIT) backwards trajectories, and the intensity as well as duration of heavy rainfall events. We find that while the synoptic-scale pattern that produces ARs is similar to other AR studies, there are some differences in the synoptic-scale environments consistent with the study of inter-annual variability in this region. Also, while much of the moisture ingested by ARs comes from the Gulf and Caribbean, if moisture comes from the Atlantic region there is a potential for larger rainfall events. Finally, an analysis of upper-air soundings shows some key differences between warm and cold season ARs, and possibly inter-annual variations as well.

KEYWORDS

atmospheric dynamics, atmospheric rivers, atmospheric water vapour, ENSO, models, satellite, seasonal variability, upper-air sounding

1 | INTRODUCTION

Since the onset of the remote sensing era, there have been many advances in the analysis and forecasting of high-impact weather, especially heavy precipitation events (e.g., Stephens and Kummerow, 2006; Bosart *et al.*, 2017; Kastman *et al.*, 2017a; 2017b). There is still much work needed, however, in order to understand better the dynamics of these atmospheric phenomena (e.g., Lupo *et al.*, 2016; Kastman *et al.*, 2017a; 2017b). The purpose of this study is

to garner a better understanding for the antecedent factors that contribute to or are associated with heavy rainfall events across the North-Central Mississippi River Valley. In particular, we examine the possible influence of atmospheric rivers (ARs; e.g., Newell *et al.*, 1992; Lavers and Villarini, 2013) connected with these heavy rainfall events. ARs can be responsible for a large portion of the monthly and seasonal rainfall for the region as implied by Lavers and Villarini (2013). The contribution of ARs to monthly and seasonal precipitation will be quantified for our study region

since they can cause widespread flash flooding (e.g., May 7, 2000) or prolonged flooding (e.g., December 26–27, 2015). The latter event led to the destruction and closure of major interstates, in addition to economic damage and even loss of life. The occurrence and recurrence of similar events are studied routinely (e.g., Thielen *et al.*, 2010; Steinschneider and Lall, 2015).

Although there is a history of studies examining moisture plumes (e.g., Thiao *et al.*, 1995; Dirmeyer and Kinter III, 2010; Lavers and Villarini, 2013) for regions located in the United States, more recent studies have been performed in order to take advantage of data sets with better spatial resolution. Dirmeyer and Kinter III (2009) examined the causes of the May and June 2008 flooding event that occurred across the Midwest region. They found that the preceding seasons were anomalously wet and the situation was similar to the widespread 1993 Midwest United States flooding event (e.g., Junker *et al.*, 1999). An extended study by Dirmeyer and Kinter III (2010) found that anomalously wet spring and summer months (including 2008) in the upper Midwest resulted from, at least partially, a long narrow fetch of low and mid-level moisture originating in the Caribbean and Gulf of Mexico and extending over the Mississippi Valley Region. Dirmeyer and Kinter III (2009), Dirmeyer and Kinter III, 2010) associated this plume with a persistent extension of the Bermuda High into the Southeast United States and the former study dubbed these ARs the “Maya Express.” Later, Lavers and Villarini (2013) demonstrated that a high proportion of flooding events in the North-Central Mississippi River Valley region are associated with ARs. Nakamura *et al.* (2013) found that anomalous water vapour transports into the Ohio River Basin by the large-scale (climatological) flow was responsible for flooding events. All these studies examine relatively long time periods and the composite impact of moisture transport. Moore *et al.* (2012) examined the role that an individual AR played in a flooding event within the Ohio River Valley Basin during May 1–2, 2010. Recently, Mahoney *et al.* (2016), Debbage *et al.* (2017), and Miller *et al.* (2018) found that the contribution of ARs to heavy rain events in the Southeast United States varies annually. Debbage *et al.* (2017) examined the occurrence of ARs along the Gulf and Southeast United States coasts including the inter-annual variability of ARs. Additionally, Miller *et al.* (2018) examine the occurrence of AR associated with heavy rainfall over a 5-year period in western North Carolina.

In order to improve the understanding of the dynamics associated with heavy rainfall events, it is imperative to acknowledge recent progress of atmospheric research with regard to ARs through the use of models that track air parcel trajectories or examine upper-air soundings. The first part of this work builds on previous studies, some of which focused on analysing atmospheric phenomenon using tools such as upper-air soundings. This work also examines heavy rainfall

events in our region associated with ARs and compare with previous work highlighting the impacts of landfalling ARs (Thiao *et al.*, 1995; Bluestein and Banacos, 2001; Dirmeyer and Kinter III, 2009; 2010; Dettinger *et al.*, 2011; Moore *et al.*, 2012; Nakamura *et al.*, 2013; Mahoney *et al.*, 2016; Miller *et al.*, 2018).

The structure of this paper is as follows; section 2 discusses the data used and methods that were implemented in this work. In section 3, the first subsection discusses the analysis of heavy rainfall events that occurred concurrently with landfalling ARs, including the synoptic-scale environment, and the second discusses the variability (seasonal and inter-annual variability, e.g., El Niño–Southern Oscillation [ENSO]) of the synoptic-scale environments. The third subsection encompasses the findings associated with HYSPLIT air parcel trajectories analysed for the respective heavy rainfall events, and the last subsection reviews the results garnered from the analysis of upper-air soundings. The HYSPLIT trajectory utility (Stein *et al.*, 2015) is used in many studies to track air parcels within atmospheric data sets such as output produced by a model (e.g., Stunder *et al.*, 2007), and is user-friendly. The results found in this study for inter-annual variability (ENSO) will be put in the context of other meteorological studies for this region (e.g., Berger *et al.*, 2002; Lupo *et al.*, 2012; Newberry *et al.*, 2016) including studies of AR variability (e.g., Guan and Waliser, 2015). Analysis of the upper-tropospheric forcing associated with jet streaks as well as synoptic features associated with ARs in our region has not been investigated fully. The final section presents discussion of the results and conclusions.

2 | DATA AND METHODOLOGY

2.1 | Data

The results presented below will help provide further insight into the implications and future operational purposing of information acquired for individual AR using newly developed meteorological tools. The unique aspect of this paper is to examine different synoptic and dynamic scenarios involving individual ARs, and the relationship to heavy rainfall events (>50.8 mm in 24 hr) occurring across the study region. The study region includes the Springfield (SGF) and St. Louis (LSX) Missouri National Weather Service (NWS) Forecast Offices (WFOs) and the territory over which weather forecasts are issued (in the United States these are called County Warning Areas [CWAs]) (Figure 1). The authors are not aware of another study that examines ARs impacting this region using the analysis performed, including analysis using the HYSPLIT trajectory utility. Typically, ARs have been studied in high-impact precipitation events across the western United States (e.g., Neiman *et al.*, 2008) or along the Gulf Coast and southeastern United States (e.g., Mahoney *et al.*, 2016; Debbage *et al.*, 2017; Miller

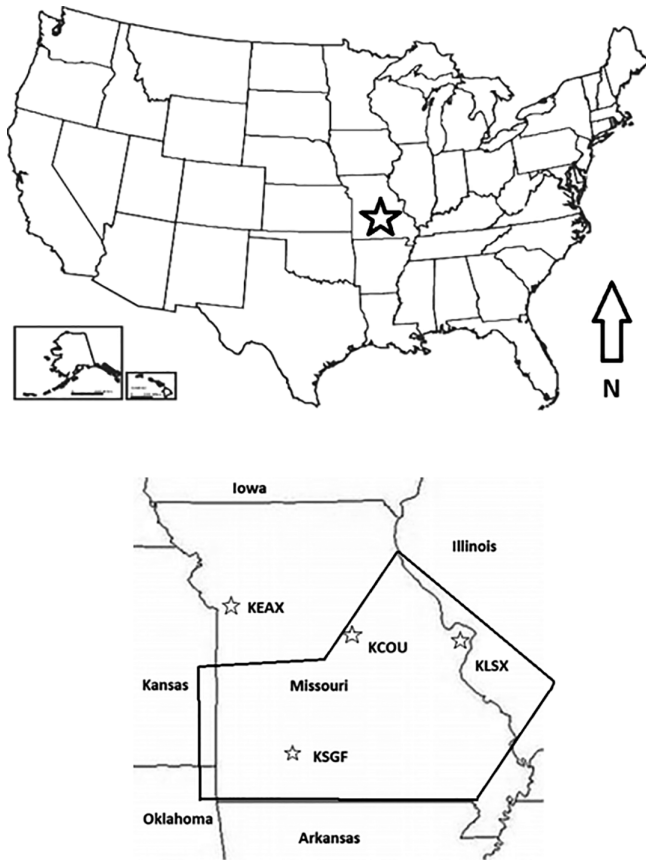


FIGURE 1 The study region for this work. The top is a map of the United States with Missouri marked with a star. The bottom is the state of Missouri with key cities. The lines show the general area covered by the SGF and LSX CWAs. The scale distance is 391 km from KEAX to KLSX

et al., 2018), but not in such detail across our study region. The rainfall events and AR studied here occurred during the period between 2000 and 2015.

Two data sources used to study ARs were the Special Sensor Microwave Imager Sounder (SSMIS) (which is a satellite-based passive microwave radiometer) and the Morphed Integrated Microwave Imagery at the Cooperative Institute for Meteorological Satellite Studies (CIMSS)–Total Precipitable Water (MIMIC-TPW) satellite-derived product (Cooperative Institute for Meteorological Satellite Studies (CIMSS), 2017). The MIMIC-TPW uses retrieved total precipitable water (integrated water vapour [IWV]) values at 0.5° latitude/longitude resolution at 15-min intervals based on an algorithm developed by Alishouse *et al.* (1990). These data were available from 2005 to 2015. This algorithm derives these values from a linear function of 19, 22, and 37 GHz brightness temperatures available from passive microwave sensors aboard several polar orbiting satellite platforms. These polar orbiting satellite platforms include real-time data from the Special Sensor Microwave Imager (SSM/I) sensor on the Defense Meteorological Satellite Program (DMSP-13/14) satellites as well as the Advanced Microwave Sounding Radiometer (AMS-R-E) sensor aboard the Aqua satellite (Wentz *et al.*, 2017). These data were used

from the period 2000–2015, which overlapped the period noted above for the CIMSS MIMIC-TPW data.

Lastly, the North American Regional Reanalyses (NARR; Messinger *et al.*, 2006) were used to investigate the synoptic-scale environment as well as providing the integrated water vapour transport (IVT) values used to identify the character of the ARs from 2000 to 2015. The IVT is the product of specific humidity and the horizontal wind integrated through the depth of the troposphere (e.g., Neiman *et al.*, 2008). The NARR data set is an extension of the National Centers for Environmental Prediction/National Center for Atmospheric Research (NCEP/NCAR) reanalyses (Kalnay *et al.*, 1996). These data are available at $1.0 \times 1.0^\circ$ latitude/longitude grids eight times daily, and these are sufficient for calculating the size of an AR and the synoptic-scale analysis performed below. This resolution is finer scale than available from other data sets (e.g., NCEP/NCAR or ERA-Interim) used to study synoptic-scale phenomena. The variables used were sea level pressure (hPa), 850 and 500 hPa height (m), 850 and 300 hPa vector wind (m/s), IVT ($\text{kg m}^{-1} \text{s}^{-1}$), and precipitable water (PW) (mm). These variables were examined over the lower 48 contiguous states North America from approximately $25\text{--}50^\circ\text{N}$ and $130^\circ\text{--}65^\circ\text{W}$ longitude. The daily and monthly precipitation data (inches) is available through the National Weather Service website at the SGF and LSX WFO (National Weather Service, St. Louis Office, 2017) for the period 2000–2015, and were converted to mm. Only rainfall events of greater than 50.8 mm in 24-hr were examined in this study.

2.2 | Identification of ARs impacting the region

As coined by Newell *et al.* (1992), ARs are characterized as long/narrow corridors of deep water vapour that transport moisture from the tropics, across the mid-latitudes, and towards the poles. The Glossary of Meteorology (American Meteorological Society, 2017) defines these as a transient moisture transport corridor at least 850-km wide and we use this generic width definition. The second criterion chosen for the identification of AR was the maximum IVT, which had to be associated with transports greater than $500 \text{ kg m}^{-1} \text{ s}^{-1}$ used by Mahoney *et al.* (2016) and others for the study of ARs east of the Rocky Mountains. This value must have been maintained for at least 24 hr as it impacted the study region (Figure 1) and must have been associated with heavy (>50.8 mm) rainfall events. These events are typically associated with flooding events across the region of study (Kastman *et al.*, 2017a; 2017b), and represent the largest 24-hr rainfall events during the study period (two events per year). Using this criterion, 15 AR events were identified over the 15-year period and this result is consistent with those used by many recent studies (see Debbage *et al.*, 2017). During the same time period, 29 events total produced more than 50.8 mm of rainfall in 24 hr, but 14 of these rainfall did not meet the definition of an AR as set above. Those that did not meet the

criterion failed the AR width criterion, the duration criterion, or both. Additionally, the minimum duration specified above is similar to Debbage *et al.* (2017) whose duration time was specified as 48 hr, but longer than Miller *et al.* (2018) who specified a minimum duration of 12 hr. The definition of the former and that used in this study clearly identify synoptic-scale phenomena (about 1–7 days). The AR intensity was defined as the largest value of IVT along the AR axis derived from the satellite technology.

The AR width (width_{AR}) was estimated as the width in longitude of the AR event at a given latitude using the $250 \text{ kg m}^{-1} \text{ s}^{-1}$ contour on either side of the moisture plume using the NARR data set. The number of longitudes was converted to km using geometry:

$$\text{width}_{\text{AR}}(\text{km}) = \text{longitudinal width} * 111.15 \text{ km/deg} * \cos(\phi) * \cos(\text{ArO} - 180), \quad (1)$$

where the latitude (ϕ) was assigned based on the location of the AR at the widest point between the Gulf Coast and our region. Using Equation 1, the mean width of the ARs identified was 1,169 km and the narrowest was 866 km.

Alternatively, the length of an AR was calculated in a similar manner by estimating the latitudinal distance from the polewards location on the axis to the most equatorwards location and multiplying by 111.15 km/deg. In order to account for orientation, the value was modified by dividing the latitudinal distance by $\cos(\text{ArO} - 180^\circ)$. While these calculations do not account for curvature of the Earth, the mean length of the 15 ARs studied was 3,182 km. The results of Neiman *et al.* (2008) and others suggested that the ratio of AR length to width is more than 2:1, and the result found above was consistent with these other studies. Again, the width calculated above may be overestimated likely since it was defined as the widest width of an AR equatorwards of our region over land. However, our length and width criterion including their ratio is consistent with many published definitions (see Debbage *et al.*, 2017).

In studying ARs with respect to spatial extent, past studies (e.g., Knippertz *et al.*, 2013) found that landfalling ARs often had greater impact during events in which the incoming moisture plume was wider-than-average. The prevailing reason for why wider ARs are more impactful is that during the landfall of a wider AR, areas, such as the North-Central Mississippi River Valley, experience heavier rainfall over a larger spatial domain due to the greater coverage by the water vapour plume (Wang and Chen, 2009). This is reduced substantially during the landfall of ARs with narrower moisture plumes due to the limited horizontal extent of the deepest atmospheric water vapour content (Knippertz *et al.*, 2013).

2.3 | HYSPLIT, upper-air soundings, and ENSO definition

The results section discusses findings from the analysis of backwards air parcel trajectories generated by HYSPLIT.

These backwards air parcel trajectories were generated via customized, user defined, specifications integrated into the HYSPLIT algorithm designed for the analysis of atmospheric fluid properties. The HYSPLIT system uses a hybrid approach between the Lagrangian and Eulerian frame of reference. The former is used for the calculation of advections and diffusion, while the latter is used for air pollution modeling, and more details can be found on the model website (Air Resources Laboratory (ARL), 2017).

The HYSPLIT was implemented to generate ensemble backwards air parcel trajectories ending at the 1,500, 3,000, and 4,500 m, which are close to the 850, 700, and 600 hPa mandatory levels near the centre of the polygon in Figure 1. These levels were chosen since the former level resides near the top of the planetary boundary layer, and the latter two are where clouds would be expected to form. This location was chosen to represent a common destination for the parcels just upstream of where the precipitation was measured. All three layers were within the deep moist layer for each event during the 24-hr lifecycle. The HYSPLIT vertical motions prior to the occurrence of ARs were calculated gridded model vertical motions and isentropic vertical motions. Backwards parcel trajectories were calculated during the 120 hr preceding the event occurrence with heavier weight being placed on the model vertical velocity calculation method. It is important to note that the vertical motion used is the model calculated omega field (Air Resources Laboratory (ARL), 2017) (i.e., from the Global Deterministic Assimilation System [GDAS]) with 3-hourly and 1° latitudinal/longitudinal resolution data, available since 2005. From 1997 to 2004, the Eta-based Data Assimilation System (EDAS) with 3-hourly, 80-km resolution data (Air Resources Laboratory (ARL), 2017). The HYSPLIT allows for the inclusion of up to 24 parcel backwards trajectories ending at one location, and each member is generated by offsetting the initial meteorological data by a fixed amount at the trajectory start.

The upper-air soundings were studied during the 48-hr preceding the period of heaviest rainfall during each AR event. These soundings were acquired from three sources including the Plymouth State University Weather Center website thermodynamic diagram generator, the upper-air soundings from the University of Wyoming Weather (2017), and the SPC Severe Weather Event Archive Database (2017). There were utilized for comparison due to the different vertical resolutions available for each data set. The motivation for analysing the upper-air sounding evolution during the 48 hr preceding each event was to assess the vertical wind profile configuration prior to the heavy rainfall and then during each event.

The distribution of the respective post-2000 ENSO phases is shown in Table 1, and ENSO is defined using the Japanese Meteorological Agency (JMA) criterion (Center for Ocean and Atmosphere Prediction Studies (COAPS), 2017).

TABLE 1 List of ENSO years 2000–2015: see Center for Ocean and Atmosphere Prediction Studies (COAPS) (2017) for definition, ENSO year begins October 1 of the given year (see section 2)

El Niño	Neutral	La Niña
2002	2000–2001	1999
2006	2003–2005	2007
2009	2008	2010
2014–2015	2011–2013	

This definition has been used by many studies of inter-annual variability in the broader region (e.g., Newberry *et al.*, 2016, and references therein) and will facilitate comparing our results with those studies. In Table 1, the ENSO year 1999 begins with October 1, 1999 and ends on September 30, 2000 (see COAPS website for this convention). Also, the studies of Dirmeyer and Kinter III (2009; 2010) and Nakamura *et al.* (2013) suggest that the occurrence and location of individual ARs may depend on the large-scale flow regime, which is in turn impacted by ENSO in this region (e.g., Lupo *et al.*, 2012). Lastly, Guan and Waliser (2015) examine the inter-annual variability in the occurrence of ARs globally during the period from 1997 to 2014 and these will be compared to our results.

3 | RESULTS AND DISCUSSION

3.1 | Atmospheric rivers: Regional climatological considerations

The climatological examination of post-2000 heavy rainfall events linked to ARs showed the following results. In this section, the contribution to AR-related heavy rainfall and the relationship to AR intensity (i.e., the deepest atmospheric water vapour column transported into a given region) was examined. A plan view of a typical AR event impacting the study area is shown in Figure 2, and this diagram was inspired by Moore *et al.* (2012) which showed an Ohio River Valley AR from early May 2010. A list of the events studied is found in Table 2.

One of the motivations for studying ARs was that they can be responsible for a significant portion of the region's monthly or seasonal rainfall totals as implied by Lavers and Villarini (2013). The AR generated precipitation was quantified by dividing the AR precipitation by the mean 1981–2010 monthly and seasonal climatological precipitation for SGF and LSX. The ARs listed in Table 2 were responsible for at least 40% of the precipitation for a given month at the SGF and LSX WFOs (Event 4) to more than one and a half times (160%, Event 3) the monthly mean precipitation. The average contribution using these 15 events to the total monthly precipitation was 67%. Events 3 (61%), 4, and 13 (15%) represented also the extremes for their respective seasons at the SGF and LSX WFOs, and the average seasonal contribution was 30%. These results are

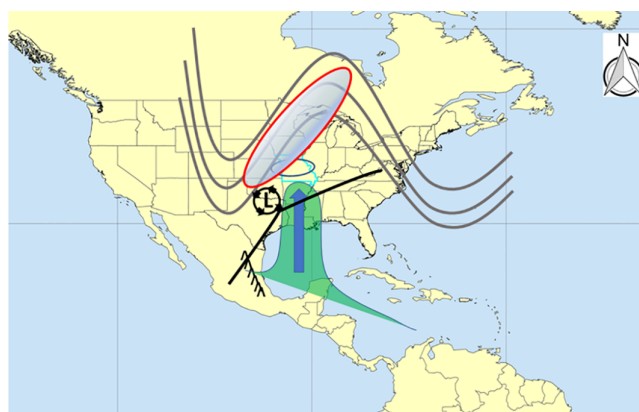


FIGURE 2 Plan view of a typical AR in the study region and inspired by Moore *et al.* (2012). Our study area as in Figure 1 is circled in black. The dark green shows the approximate path of a typical IVT precipitable water plume for a heavy rain event, the translucent green is IVT greater than $500 \text{ kg m}^{-1} \text{ s}^{-1}$, and the blue arrow is the moisture transport. The Sierra Madres are denoted with the black “tents” in Mexico, the grey lines are the 500 hPa trough and ridge, and the grey translucent oval represents the 300 hPa flow. The fronts and pressure systems are denoted with plain black lines and an L [Colour figure can be viewed at wileyonlinelibrary.com]

qualitatively similar to the results of Lavers and Villarini (2013) and they found that ARs were responsible for 30% or more of the flooding events in this region from 1980–2011. By comparison, Mahoney *et al.* (2016) found that 40% of Southeast United States heavy rainfall events were associated with ARs. Additionally, winter season ARs generally provided larger fractions of the monthly and seasonal precipitation (Table 2). This is also consistent with Lavers and Villarini (2013) who found a larger proportion of AR generated floods in the region and Mahoney *et al.* (2016) who found a larger contribution from ARs to Southeast United States heavy rainfall events outside the summer season.

While the seasonal contributions in this study are not as large as those for the Northwest United States (which can be more than 50%, e.g., Dettinger *et al.*, 2011), comparing our Figure 2 to Neiman *et al.* (2008, fig. 17) shows that the topography is different for our study region. Whereas Pacific region ARs collide with the Coast Range mountains such as the Sierra Nevada or Cascade Mountains in the west, the topography south of our study region acts to funnel moisture into the area as stated also by Moore *et al.* (2012).

An analysis of AR events with respect to AR intensity generated the following result (Figure 3). An AR intensity scatter plot was studied to assess the presence of statistical correlation and significance between IVT and IVT anomalies with the AR associated rainfall events. Figure 3 suggested that AR with stronger IVT and IVT anomalies produced higher rainfall events, and the Pearson correlation coefficient was 0.53 and 0.49, respectively. Both were significant at the 95% confidence level when testing the correlation using a one-tailed significance test. Eleven of the fifteen data-available events occurred in association with AR intensities (IVT) ranging between 500 and $850 \text{ kg m}^{-1} \text{ s}^{-1}$ and 12 of

TABLE 2 List of AR events with respect to ENSO

Event number	Date	ENSO phase	Synoptic type	IVT anomaly ($\text{kg m}^{-1} \text{s}^{-1}$)	Month (%)	Season (%)
	Jun 12, 2003	El Niño	PR	+305.0	43	17
1	Nov 30, 2006	El Niño	RD	+410.0	69	24
2	Dec 26, 2015	El Niño	SW	+600.0	160	61
3	May 12, 2002	Neutral	PR	+405.0	40	15
4	Jan 4, 2004	Neutral	PR	+570.0	119	37
5	May 27, 2004	Neutral	PR	+505.0	46	18
6	Jun 11, 2005	Neutral	PR	+255.0	51	20
7	Sep 14, 2008	Neutral	PR	+780.0	48	18
8	Apr 18, 2013	Neutral	PR	+730.0	50	16
9	May 7, 2000	La Niña	PR	+310.0	43	17
10	Jun 24, 2000	La Niña	PR	+410.0	45	18
11	Feb 5, 2008	La Niña	SW	+600.0	83	26
12	Mar 18, 2008	La Niña	PR	+660.0	56	15
13	May 26, 2008	La Niña	SW	+305.0	90	35
14	Sep 1, 2014	La Niña	PR	+500.0	54	20

Note. Number of the AR event is given in the first column, then event date, ENSO phase, synoptic type following Berger *et al.* (2002), the largest IVT anomaly contour ($\text{kg m}^{-1} \text{s}^{-1}$) in the study region, and percentage contribution to the monthly and seasonal LSX precipitation in subsequent columns, respectively. The synoptic type PR, RD, and SW are progressive trough, rapid deepening, and southwest low, respectively.

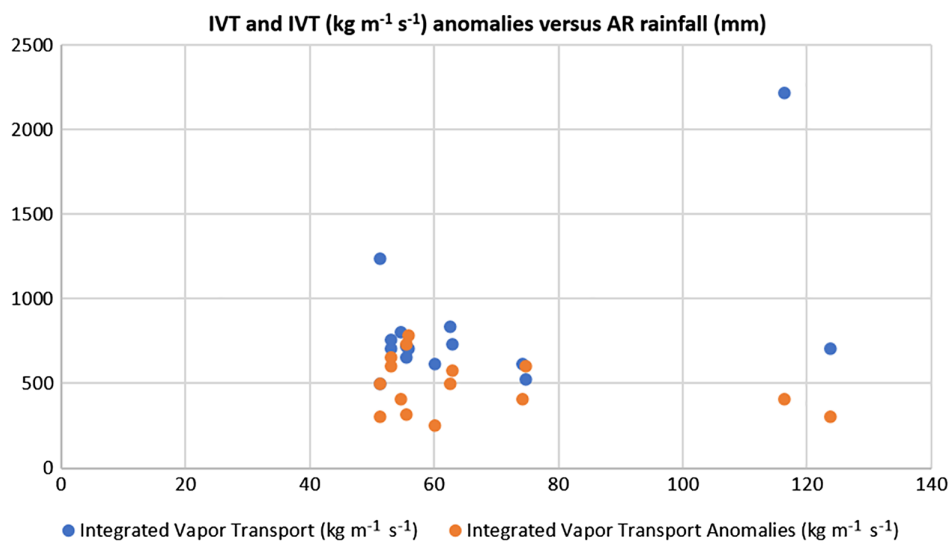


FIGURE 3 Scatter plot of atmospheric river (AR) intensities as measured by IVT (blue) and IVT anomalies (orange) ($\text{kg m}^{-1} \text{s}^{-1}$, ordinate) for all 15 events with event rainfall totals (mm) (abscissa) [Colour figure can be viewed at wileyonlinelibrary.com]

15 with IVT anomalies from 250 to $600 \text{ kg m}^{-1} \text{s}^{-1}$ (Figure 3).

3.2 | Synoptic analysis and seasonal and inter-annual variability

Berger *et al.* (2002) subjectively classified the 500 hPa flow for winter season heavy snowfall events (398 events) in Missouri over a 50-year period into four general synoptic types, progressive trough (PR), southwest low (SW), northwest low (NW), and rapid deepening lows (RD). Each type was distinct from the others with the exception of the SW and RD (see Berger *et al.*, 2002, fig. 2). While the SW and RD types are characterized by a deep trough over the Southwest United States (see Figure 4), these two differ by the

deepening rate of the surface cyclone which should meet the published criterion for explosive development (see Sanders and Gyakum, 1980). PR are characterized by lower-amplitude troughs that move across the United States prior to, during, and after the event in our region (see Figure 5).

Berger *et al.* (2002) found that PR events were the most common cold season (October–April) type (47.7%), SW events were second most common (26.7%), followed by NW events (17.3%), and RD events were the least common (8.3%). An analysis of warm season (May–September) events from 2000 to 2015 demonstrated that PR events were most common (68.5%), followed by NW events (19.0%) and SW events (10.5%), while RD events were the least common (1.5%). SW and RD events were characterized by southwest flow over the region at 500 hPa and the 500 hPa trough

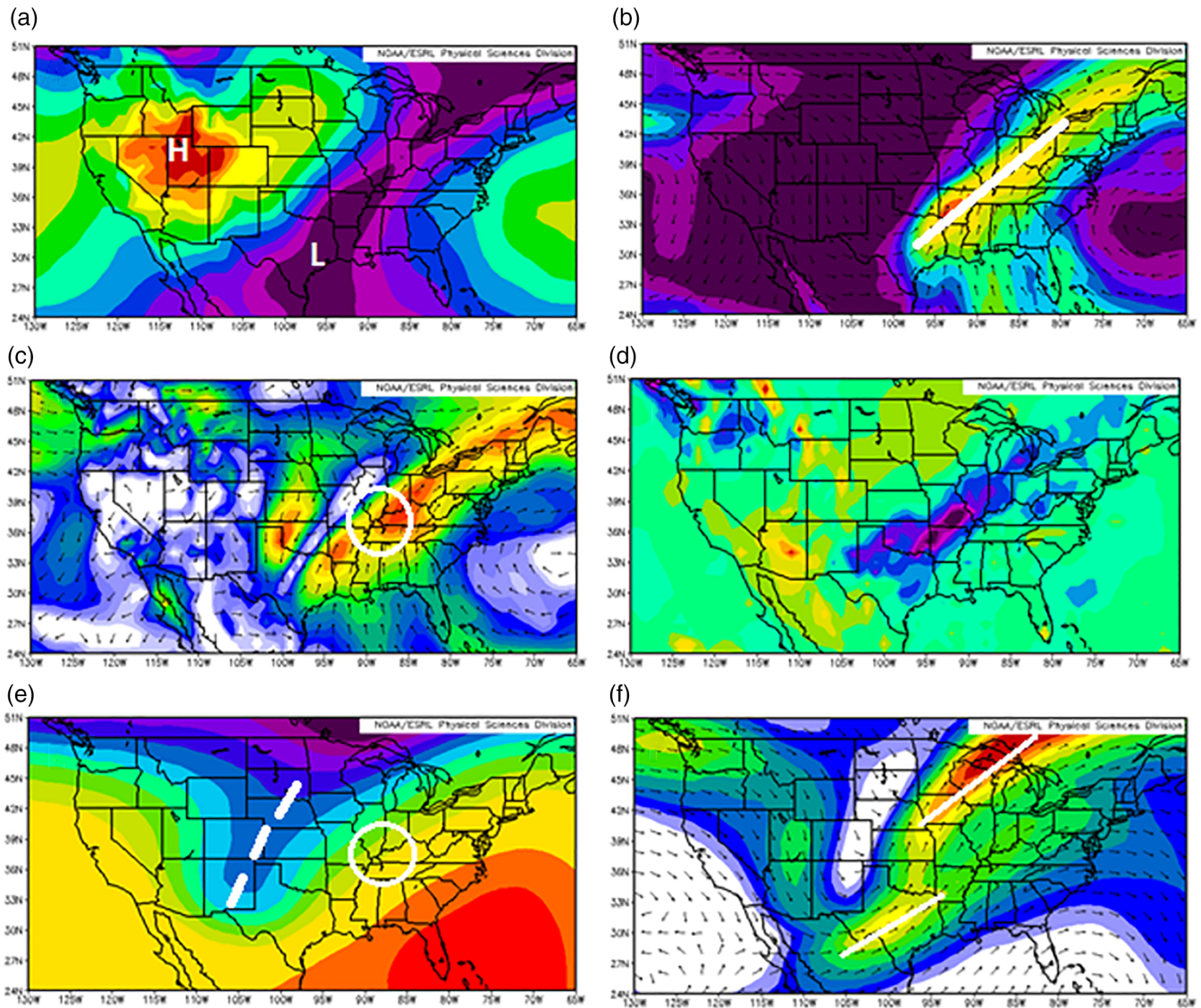


FIGURE 4 The mean (a) sea level pressure (hPa), (b) IVT ($\text{kg m}^{-1} \text{s}^{-1}$), (c) 850 hPa vector winds (m s^{-1}), (d) 700 hPa vertical motion ($\mu\text{b/s}$), (e) 500 hPa height (m), and (f) 300 hPa vector winds (m/s) for November 30, 2006 (Event 2). The contour shading intervals were (a) 4 hPa, (b) $50 \text{ kg m}^{-1} \text{s}^{-1}$, (c) 1.0 m/s, (d) $0.5 \mu\text{b/s}$ (cold colours are negative), (e) 60 m, and (f) 2.5 m/s. The positions of highs (H) and lows (L) are marked, and trough lines and jet axes are identified as white dashed and solid lines, respectively. Credit: Earth System Research Laboratory, NOAA Physical Sciences Division (<https://www.esrl.noaa.gov/psd/cgi-bin/data/getpage.pl>) [Colour figure can be viewed at wileyonlinelibrary.com]

remained west of the region during the event. PR events were characterized by a mobile 500 hPa trough that propagated into the region during the event lifecycle, and a NW event was characterized by northwest flow at 500 hPa and the main trough axis was located east of the region (Berger *et al.*, 2002).

Most (11/15–73%) of the ARs were PR events (Table 2), and only three (one) AR event(s) were SW (RD) events, which represents 20% (7%) of the sample. Since ARs require a significant moisture source, it was expected that there would be no AR classified as NW events. The number of AR events classified as PR events was higher than the Berger *et al.* (2002) cold season climatology or a combination of the cold season and warm season PR events (58%). The combined number of SW and RD events (27%) of this small sample was consistent with the similar number for both the

warm and cold season together (24%). Thus, the higher number of PR events can be accounted for by the lack of AR events classified as NW events.

Additionally, the summer season events were accompanied by IVT anomalies less than or equal to $410 \text{ kg m}^{-1} \text{s}^{-1}$ (Table 2). This was also true for three of the four May events. This might be expected since the atmosphere is warmest during the summer season, but it also may make forecasting the events more difficult since IVT anomalies would not be an outstanding feature as it would be in the cold season. Lastly, more of the events occurred during the spring (40%) in spite of the small sample size. This result is consistent with the Debbage *et al.* (2017) result that showed Western Gulf ARs were most frequent during the spring season. All of the spring season events in Table 2 would be considered Western Gulf AR in Debbage *et al.* (2017).

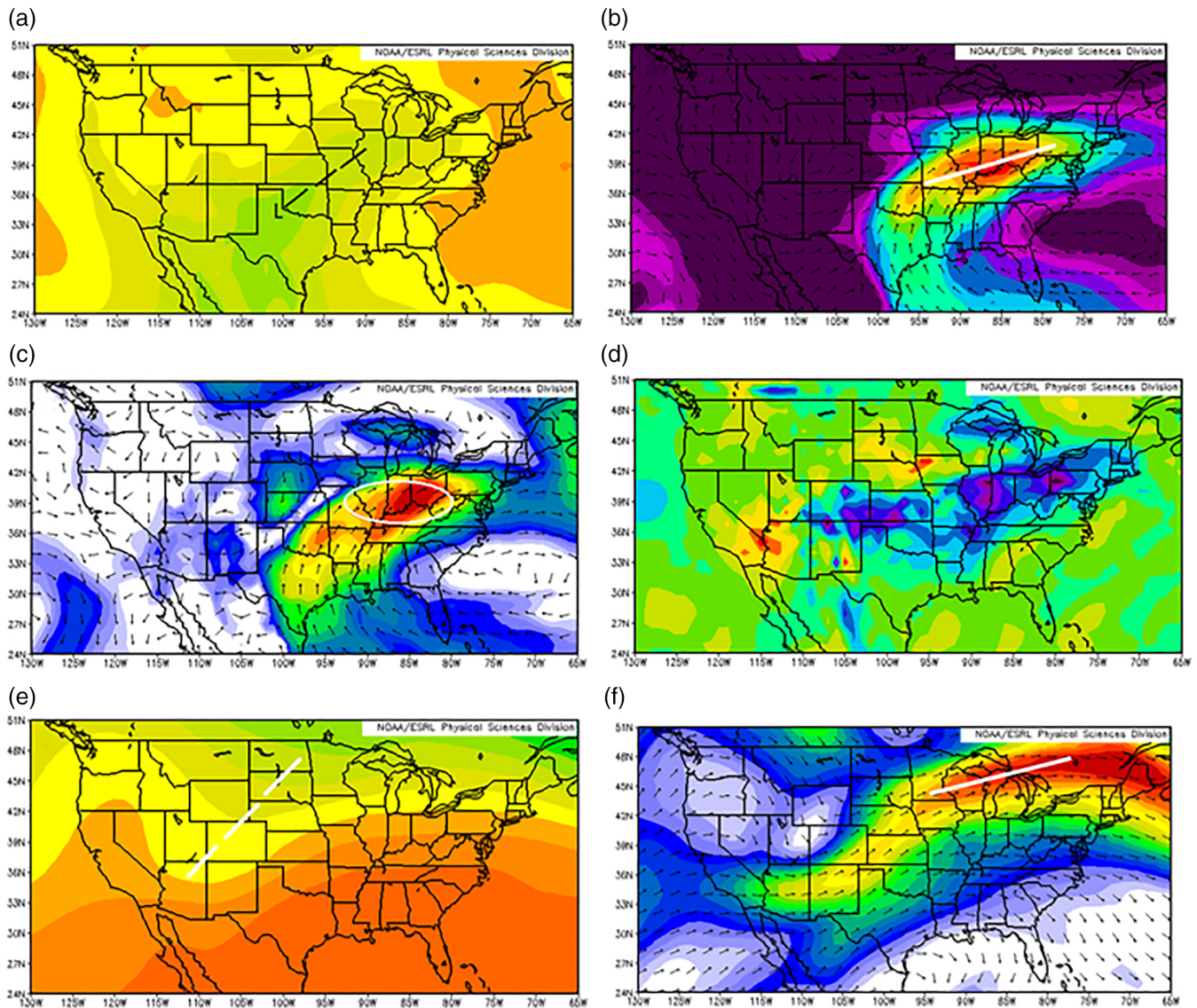


FIGURE 5 As in Figure 4, except for May 12, 2002 (Event 4) [Colour figure can be viewed at wileyonlinelibrary.com]

Among the 15 AR events examined using the MIMIC-TPW product (Table 2) only three events occurred during El Niño years and six events occurred during La Niña years and Neutral years, respectively. Note that three of the six La Niña events were associated with a wet spring that resulted in the widespread flooding of May 2008 studied by Dirmeyer and Kinter III (2009) and Dirmeyer and Kinter III (2010). Additionally, two La Niña ARs occurred during May and June 2000. The occurrence of multiple AR events during these years may be a reflection of the large-scale flow being more conducive for repeated occurrences, but more research would be required to support this point. Also, while this sample size is small, there were some outstanding features associated within each class of event. Three events were chosen for synoptic analysis that most typified their ENSO category with respect to the placement of the relevant surface and upper-air features, the location and orientation of the PW plume, and the relative size of the PW anomaly in the study region.

Figure 4 shows Event 2, which was the only RD event, and according to Berger *et al.* (2002) RD events were similar to SW events except for the deepening rate of the surface cyclone. During this event, the surface cyclone deepened 17 hPa from 1200 UTC 30 November to 1200 UTC December 1, 2006. At this latitude, the cyclone deepened at a rate of 1 Bergeron (Sanders and Gyakum, 1980). There was no closed surface feature yet at 0000 UTC 30 November (Figure 4a), and the axis of highest IVT values was south and east of the region (Figure 4b). This positioning was similar for all three El Niño events, but for only two other events in La Niña or Neutral categories was the PW axis similarly oriented. This more eastwards location for the main moisture axis during El Niño years is consistent with Lupo *et al.* (2012) who studied the inter-annual variability of dew points over a 60-year period for a region that includes the SGF and LSX CWAs. They found that the 850-hPa flow was located more over the western Gulf of Mexico. Examining Figure 4c shows that there was strong south-

southwesterly flow associated with a low-level jet (LLJ) on the upstream side of the trough at the 850 hPa and more southwesterly flow at 500 hPa (Figure 4e) implying the advection of warm moist air into the region (Figure 4c, circle). In this case, Figure 4f showed that there were two jet maxima present such that the quadrants favouring upwards motion were co-located over the study region and the southern plains, a common configuration for heavy rainfall events in this region (Kastman *et al.*, 2017a). Additionally, Figure 4d showed strong upwards vertical motions over the study region and southern plains. Thus, the conditions typically associated with strong cyclone development (Lupo and Smith, 1995, and references therein) were present in this case.

Examining Event 4 which typified Neutral events (Figure 5), the surface low was located over Texas (Figure 5a), and the axis of the largest IVT was over the study region (Figure 5b). Event 4 was a PR event. These figures were similar to the analogous features for the La Niña events (represented by Event 14—a SW event—Figure 6a, b), except that the surface low was located at least 100 km further northwest (over the Oklahoma panhandle and in Kansas). Each of these cases demonstrates the importance of the LLJ in carrying deep moisture into the region. Also, for five of the six Neutral events, the atmosphere over the Gulf of Mexico was relatively dry (see, e.g., Figure 5 and also precipitable water values). This is consistent with Lupo *et al.* (2012) who found that the strongest 850 hPa flow was located 5–10° longitude further west during these years (see Figure 5c). At 850 hPa, the trough with a strong LLJ located to the west of the region in Figure 1 was narrow which is more similar to the El Niño group (Figure 4c), but for the La Niña group (Figure 6c) this trough was broad covering most of the western one third of the United States. The 500 hPa heights (Figures 5e and 6e) also implied warm air advection over the study region, as the winds at this level as suggested by the height fields were more southwesterly than at 850 hPa. Additionally, Figures 5d and 6d demonstrated that there were upwards motions over the region of study and surrounding locations, while Figures 5f and 6f showed that the study region was located within the equatorwards exit region of the upper-level jet.

The synoptic orientation of upper-air features such as jet maxima can be an important consideration for the development of heavy rain events (e.g., Kastman *et al.*, 2017a, and references therein). Examining the 300 hPa wind fields associated with each event (e.g., Figures 4f, 5f, and 6f) demonstrated that all of the 15 AR events studied in Table 2 were supported by divergence aloft associated with the entrance and exit regions of jet maxima. All these events also exhibited a signature similar to the anticyclonic wave breaking scenarios studied by Bosart *et al.* (2017) for extreme precipitation events. However, in 9 of the 15 cases, the equatorwards entrance region of a jet maximum located

polewards or polewards and east of the study area was the contributing feature to upper-air divergence (Figures 5f and 6f). Five of the events resembled the coupled jet scenarios studied by Kastman *et al.* (2017a) (Figure 4f). Only one of these coupled jet scenarios was a cold season case (Event 2, Figure 4f). Finally, for one case it was difficult to determine conclusively whether the upper-air divergence was associated with the equatorwards entrance region or a coupled jet scenario.

The highest average IVT and IVT anomalies (Table 2) within the study region was observed during Neutral AR events using the NARR (1,054 and +541 kg m⁻¹ s⁻¹, respectively). A comparison to the El Niño and La Niña year events showed that the IVT were smaller (692 and 653 kg m⁻¹ s⁻¹, respectively), and the IVT anomalies were (+438 and +464 kg m⁻¹ s⁻¹, respectively). The smaller IVT observed during La Niña events is consistent with Lupo *et al.* (2012) who found that the surface dew points and relative humidity was lowest during these years. However, it is conceded that the inter-annual variations found in this subsection while consistent with previously published research for this region such as Berger *et al.* (2002), Lupo *et al.* (2012), or Newberry *et al.* (2016), may not be significant at acceptable levels of statistical confidence. However, the occurrence of AR in this region were higher in La Niña years (2.0 events/year vs. 0.7 and 0.6 events/year in Neutral and El Niño years, respectively), a result consistent with those of Guan and Waliser (2015) who examined a global climatology of AR from 1997 to 2014. These case studies also showed some interesting differences between the location of some of the key surface and upper-air features. A longer time period and more events will be needed to affirm these characteristics.

3.3 | HYSPLIT: Examination of influences on air mass origination

The HYSPLIT was used to examine air mass origin and was implemented in order to generate ensemble backwards air parcel trajectories for the 120-hr period prior to all the events showing where the trajectories originate. Figure 7 shows an example for one case (Event 14), and the trajectories terminate at approximately the 850, 700, and 600 hPa levels, respectively (Figure 7a–c, respectively) as explained in section 2. Note that closer to the surface (Figure 7a) many of the ensemble members originate the air parcel in the Caribbean or Gulf of Mexico and only two in the east Pacific, while at mid-levels (Figure 7b) the air parcels originated over the Gulf of Mexico, Mexico, and into the East Pacific. At the highest level (Figure 7c), all trajectories originated over the east Pacific or Mexico. Most of the trajectories at each level (Figure 7) originated below the final level or underwent rising motion throughout the 120 hr time period.

Note that air mass origins were defined as the location of air parcels at the start of the 120-hr backwards trajectory

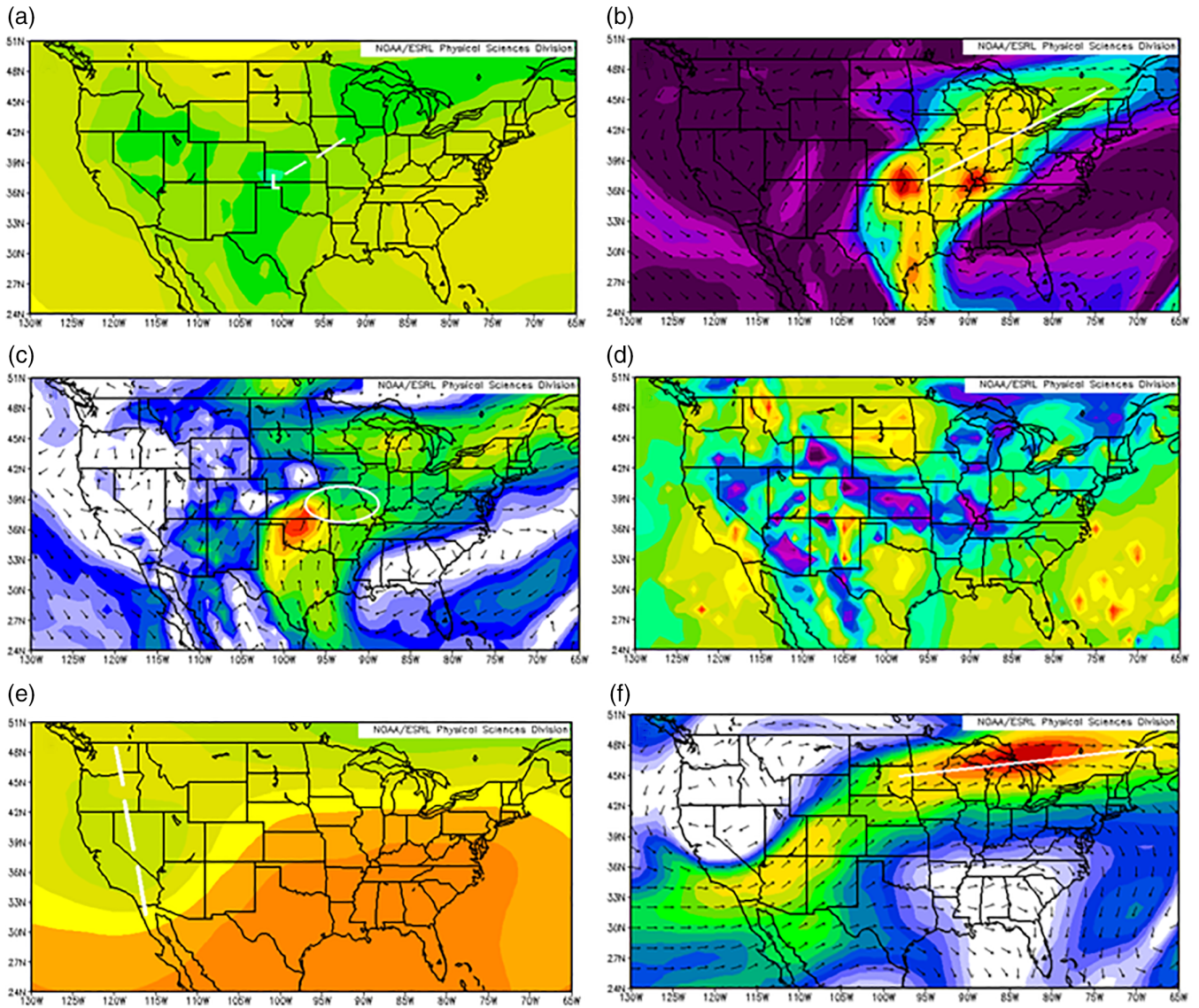


FIGURE 6 As in Figure 4, except for May 26, 2008 (Event 14) [Colour figure can be viewed at wileyonlinelibrary.com]

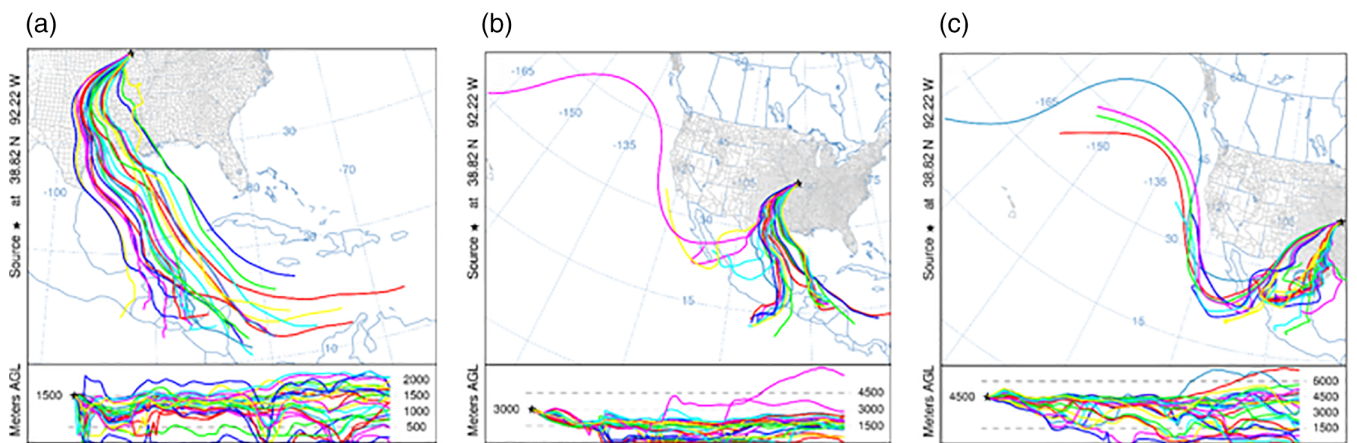


FIGURE 7 HYSPLIT utility 120-hr backwards trajectories ending at 0000 UTC May 26 (Event 14) for the (a) 1,500 m (about 850 hPa) level, (b) 3,000 m (about 700 hPa) level, and (c) 4,500 m (about 600 hPa) level. Each trajectory represents the control and individual ensemble members in 6-hr increments. Credit: National Oceanic and Atmospheric Administration (<https://ready.arl.noaa.gov/hypub-bin/trajsrc.pl>) [Colour figure can be viewed at wileyonlinelibrary.com]

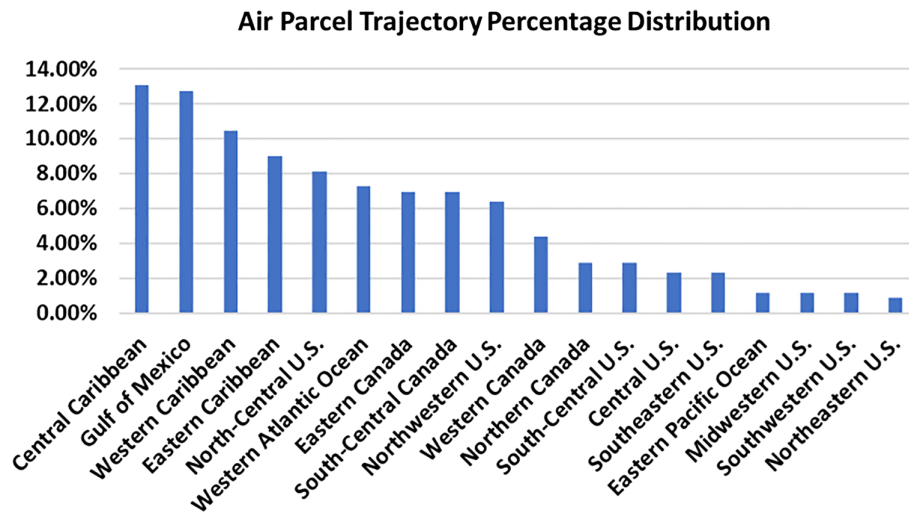


FIGURE 8 Bar plot of the air parcel trajectory origin. The percentage is calculated based on how many of the 1,080 backwards trajectories began within the given geographic area [Colour figure can be viewed at wileyonlinelibrary.com]

period emanating from the study region. Given that trajectories were analysed for the Eta and GDAS data and there were 24 trajectories at three levels per case, 1,080 individual trajectories were available for use in Figure 8 and the value shown is a percentage of the total number of trajectories. For these case studies, there was a consistent tendency for air mass origins predominantly emanating from the tropical locations for these AR which has been long recognized (e.g., Hastenrath, 1966; Hirschboeck, 1991; Donohoe *et al.*, 2013; Mayer *et al.*, 2014). Events with air mass origins from the Gulf of Mexico, Western/Central/Eastern Caribbean Sea, Western Atlantic, and Eastern Pacific constituted approximately 54% of the entire data set (Figure 8). Thus, air masses with a tropical origin had a notable influence on heavy rainfall events across the study region. In addition, events with air mass origins from either the north-central United States, the northwestern United States, and/or south-central Canada comprised approximately 21% of the entire data set. Additionally, 64% of the events covered situations defined by classic “Maya Express” AR plume interaction and/or air mass origins likely associated with synoptic-scale isentropic upglide which, respectively, facilitated heavy rainfall events.

As a landfalling AR approached a frontal boundary, the incoming moisture plume ascended over region(s) of favourable isentropic upglide. As this incoming moisture moved through the region of isentropic upglide (which often extended from the Gulf Coast region and up towards the northern Mississippi River Valley Region), enhanced rainfall rates due to overrunning in the vicinity of warm or stationary frontal boundaries was the result. An example is reflected by the generalized schematic shown in Figure 2 or Figure 9, which shows Event 3. The greatest amount of precipitation at LSX was observed in association with Event 3.

The study of the HYSPLIT ensemble backwards air parcel trajectories with respect to AR orientation (see Figures 4–6) in the study region (i.e., was the AR at an angle that was

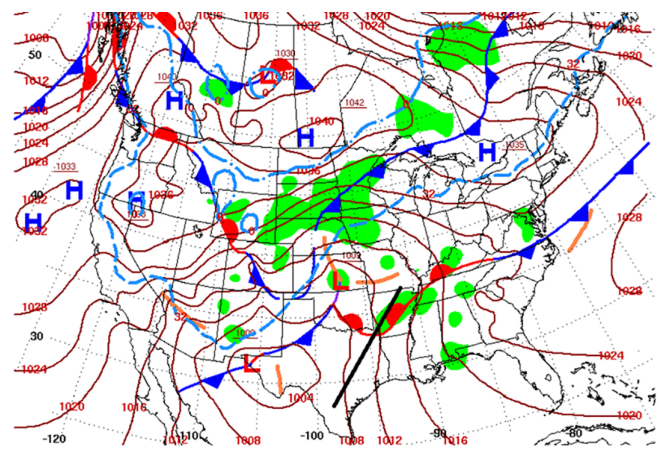


FIGURE 9 The surface weather map for 1,200 UTC December 26, 2015 (Event 3) from <http://www.wpc.ncep.noaa.gov/dailywxmap>. The black solid line represents the orientation of the AR for this event [Colour figure can be viewed at wileyonlinelibrary.com]

perpendicular to a synoptic-scale feature such as a synoptic frontal boundary or parallel to the frontal boundaries) produced the following results. The critical difference in incidence angle often determined whether the study region received larger rainfall totals (e.g., if the longer axis of the land falling AR had a more perpendicular orientation) or smaller rainfall totals (e.g., if the longer axis of the land falling AR had a more parallel orientation). A more perpendicular orientation will be associated with stronger horizontal moisture convergence. Ten of the 15 events in Table 2 had surface features more perpendicular to the AR (e.g., Figure 9), and for the top five rainfall events in Table 2 the AR were perpendicular to the surface feature (including Event 3). This was a consequence of the fact that many ARs originated from the Gulf of Mexico by way of “Maya Express” AR origins (Dirmeyer and Kinter III, 2009; 2010; Higgins *et al.*, 2011). Therefore, in situations characterized by an AR plume moving northwards from the Gulf of

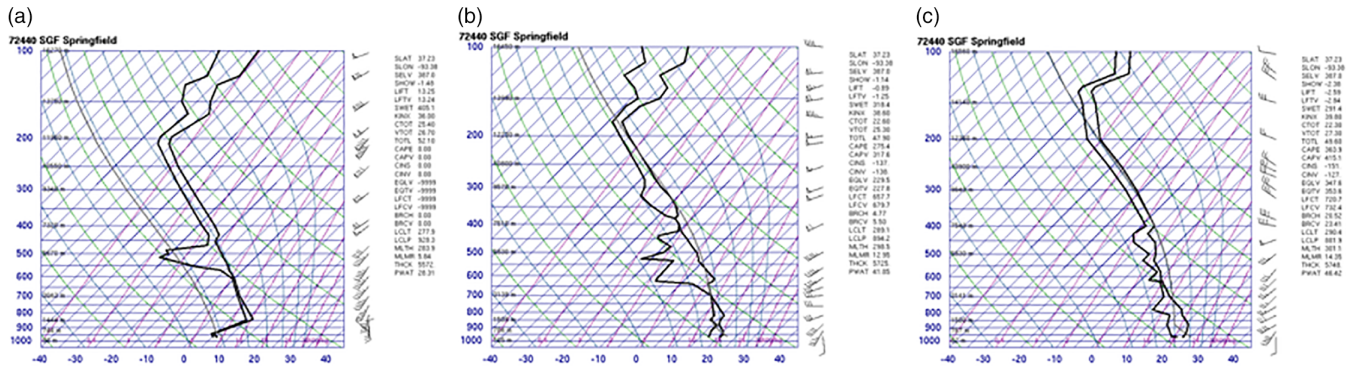


FIGURE 10 The Skew-T thermodynamic diagram for (a) Event 2 (1200 UTC November 30, 2006; Figure 4), (b) Event 4 (1200 UTC May 12, 2002; Figure 5), and (c) Event 14 (1200 UTC May 26, 2008; Figure 6) from Springfield, MO (SGF). Credit: <http://weather.uwyo.edu/upperair/sounding.html> [Colour figure can be viewed at wileyonlinelibrary.com]

Mexico, the typical progression of various synoptic-scale features aided in transporting deeper water vapour content downstream from the study region.

Another component of the HYSPLIT backwards trajectory analysis was studying the evolution of air parcel trajectory height with respect to the ocean surface. A key finding was that the optimal scenario for heavy rainfall was situations with at least 50% of the ensemble backwards air parcel trajectories positioned at or below 3,000 m (~700 hPa) during the latter 48–72 hr prior to the initial AR moisture plume landfall (e.g., Figure 7—79% of the trajectories were below 3,000 m). In many cases, the closer that air parcels moved with respect to the ocean (i.e., across the tropics) and the longer these air masses remained close to the ocean’s surface, the greater the threat for heavy rainfall potential (e.g., Hastenrath, 1966; Molinari, 1986).

3.4 | Upper-air soundings: Consideration of dynamical impacts

The upper-air soundings for the post-2000 AR associated rainfall events were examined during the 48-hr period preceding the periods of heaviest rainfall including an analysis of the wind profile (Figure 10). These profiles were examined by season and ENSO phase as in section 3.2. The

variables shown in Table 3 are convective available potential energy (CAPE), convective inhibition (CIN), the lifting condensation level (LCL), the level of free convection (LFC), and maximum sounding saturated layer depth.

A presumptive hypothesis was that stratiform precipitation would be the dominant precipitation mode for most of the events. This hypothesis appeared justified since critical CAPE values most commonly associated with convective or severe weather (i.e., greater than 2,000 J kg⁻¹, e.g., Schneider *et al.*, 2006) were not reached prior to or during most of these events (Table 3). The modest CAPE values are consistent with the Moore *et al.* (2012) AR induced flooding event. With lower CAPE values, there is often a weaker atmospheric response within the planetary boundary layer. When lower CAPE values are coupled with weak-to-moderate CIN values, this inhibits the development of deeper convection and promotes stratiform-type precipitation events. Thus it is likely that stratiform precipitation was the most common mode amongst the events.

A qualitative examination of the upper-air soundings determined whether successive upper-air soundings during the 48-hr period preceding an event had vertically veering winds or backing winds (e.g., Figure 10). These profiles were chosen to be consistent with the information shown in Figures 4–6 and before the onset of the heaviest

TABLE 3 Mean character of the profiles for the AR events including total rainfall (mm), lifting condensation level (LCL, hPa), level of free convection (LFC, hPa), surface-based convective available potential energy (SBCAPE), surface based convective inhibition (SBCIN), mean layer CAPE (MLCAPE), mean layer CIN (MLCIN), and the level (hPa) of maximum saturation (lowest dew point depression, hPa)

AR category	Total rainfall (mm)	LCL (hPa)	LFC (hPa)	SBCAPE (J/kg)	SBCIN (J/kg)	MLCAPE (J/kg)	MLCIN (J/kg)	Max saturation level
All	67.0	912	764	1,081	304	1,691	160	684
Warm season	62.9	913	756	1,418	139	1,941	158	732
Cold season	73.1	909	781	455	612	940	168	610
El Niño	83.7	938	815	483	845	959	79	712
Neutral	65.8	904	755	1,316	140	2,175	136	725
La Niña	59.7	907	748	1,146	199	1,492	229	628
CC		0.28	0.60**	-0.05	0.02	-0.22	-0.49**	-0.25

Note. The last row shows the correlation coefficient (CC) between rainfall and the other variables. A correlation significant at the 90% (95%) is denoted with an * (**).

precipitation. All of the events were associated with warm air advection and baroclinicity as shown in section 3.2 (e.g., Figures 4–6), but cases defined by stronger or persistent warm air advection (Event 2, Figures 4 and 10a) had a propensity for being associated with more warm and moist low level environments (i.e., more buoyant and often convectively unstable). For example, in Event 2 the pre-rainfall environment was associated with one of lowest Showalter Index (SI) (−1.5) and highest Severe Weather Threat (SWeaT) Index (405) values. Thus, a greater change in wind direction with height of vertically veering wind profiles prior to an event was a factor which separated the heavier (Figures 4, 6, and 10a,c) rainfall events (74.2 and 116.3 mm, respectively) from the lighter rainfall events (Figures 5 and 10b, 51.3 mm).

Another characteristic of upper-air soundings for these 15 events was deep moisture transport represented by the vertical depth of saturated sounding profiles shown in Figure 10. In particular, these sounding profiles were saturated or nearly so in the low levels, but occasionally up towards the mid-levels of the atmosphere during the 48-hr period preceding each event. Assuming that the strongest warm air advection often occurs below the 700 hPa level, but certainly within the 850–500 hPa layer, the events that had maximum saturation above the 850 hPa level often produced rainfall totals of at least 50.8 mm (or 2.00 in Table 3). Hence, the events associated with deeper maximum vertically veering sounding heights, higher maximum sounding saturation levels, and greater maximum sounding saturated layer depths were often associated with heavier event rainfall totals. However, correlations were not significant at the 90% confidence level, which may in part be due to the small sample size.

Previous work found heavier rainfall events have occurred in association with larger surface-based and mean-layer CAPE values coupled with much lower surface-based and mean-layer CIN values (e.g., Bluestein and Banacos, 2001), as a result of the greater convective instability allowing air parcels to ascend to the level of free convection (LFC) with less impediment. There was little correlation overall between surface-based CAPE and CIN versus total precipitation (Table 3) as indicated above. The CAPE value during the cold season events (October–April) were lower than those during the warm season, and this is likely due to the lower 850–500 hPa temperatures associated with cold season events (compare Figures 10a to 10b,c). However, the LCL and LFC were lower in the atmosphere for heavier AR rain events, the correlation for the latter significant at the 95% confidence level (Table 3). It is important to note that in situations with less convective instability, there were instances wherein stratiform precipitation (with possible embedded convective training) and/or elevated convection generated heavier rainfall totals (e.g., Higgins *et al.*, 2011; Kastman *et al.*, 2017b). A qualitative examination of the

RADAR images associated with these AR events (<http://www2.mmm.ucar.edu/imagearchive/>) indicates that the precipitation in five of the six cold season events was predominantly stratiform. During the warm season (May–September), four of the nine events featured convection and an additional two events featured convection embedded within a field of stratiform precipitation much like the event discussed in Moore *et al.* (2012, and references therein) or the heavy rain events of Kastman *et al.* (2017b). This was supported by the higher CAPE values during warm season events. Lastly, it was noted that there was a negative correlation between total precipitation and mean layer CAPE, and this will be explored in the future through individual case studies in order to determine if this result is a function of the small sample size. The stronger correlation (significant at the 95% confidence level) between mean layer CIN and precipitation in the warm season would be expected.

When the soundings were separated by seasons, the climatologically cooler months of the year (i.e., between October and April, six events), the lowest 100 hPa of the atmosphere were accompanied by temperatures between 0 and 15 °C (e.g., Figure 10a). During the warmer months (i.e., between May and September, nine events) the lowest 100 hPa of the atmosphere were between 15 and 30 °C (e.g., Figure 10b,c). This result is not unexpected. Also, the higher precipitation events associated with more convective precipitation featured profiles that were close to dry adiabatic, but evolve into a profile with an inversion in the lowest 100–150 hPa (e.g., Figure 10a). Lower precipitation events associated with more stratiform precipitation exhibited lapse rates that were nearly moist adiabatic from the surface into the mid-levels (Figure 10b,c). This is reflected in SBCAPE and MLCAPE that is larger for convective events than that for stratiform dominated events by about a factor of two or more (Table 3), in spite of no real seasonal difference between the location of the LCL or LFC. Thus, CAPE may be a marginally better indicator of heavy precipitation during the cold season since the largest CAPE was associated with the only convective dominated event. Additionally, the presence of an inversion for the colder season AR events may indicate the possibility of elevated convection (e.g., Kastman *et al.*, 2017b) versus surface based convection for former season events. Lastly, the maximum saturation level was about 120 hPa higher for summer season events.

When examining the values in Table 3 for the events listed in Table 2, the La Niña and Neutral year AR events showed similar mean values to each other and the total sample. These were predominantly warm season events (9 of 12). Even though there were only three El Niño year events, the mean values of the LCL and LFC were indicated at lower levels in the atmosphere (Table 3). The surfaced based and mean layer CAPE and ML CIN were lower than for the other two groups, and SBCIN was higher (Table 3).

4 | SUMMARY AND CONCLUSIONS

A total of 15 events from 2000 to 2015 were found that met the criterion for ARs using the Glossary of Meteorology (American Meteorological Society, 2017) definition for IVT and AR size that impacted a region about one-half the area of the state of Missouri. This is approximately one event per year given our criterion for AR size, intensity, duration, and associated rainfall totals. This is fewer events found by studies such as Lavers and Villarini (2013), who found an average of 13.5 events per year. However, their study region covered the United States from the Rocky Mountains to the foothills of the Appalachians. Other groups also studied larger regions (Debbage *et al.*, 2017) or used a less strict criterion (in duration, Miller *et al.*, 2018).

In section 2, the length to width ratio for AR found in this study was greater than 2:1, which similar to the ratio published in Neiman *et al.* (2008). The result is consistent with many of the definitions presented in Debbage *et al.* (2017) as well. It was found that ARs contribute to approximately 67% of the LSX monthly precipitation or 30% of the seasonal precipitation when they occur. These values were higher in the winter than in the summer since winter is the driest season in this region. This is consistent with Lavers and Villarini (2013) qualitatively as they demonstrated that a large proportion of flooding events in the region are related to AR, especially in the cold season. Additionally, we found a statistically significant correlation between rainfall at LSX and the AR intensity as measured by IVT and IVT anomalies. However, these statistical results should be viewed with caution given the small sample size.

The findings from the synoptic analysis indicated that the synoptic-scale pattern types associated with the AR events could be classified using the categorization scheme for a much longer-term cold season heavy snowfall climatology for the region (Berger *et al.*, 2002). The Berger *et al.* (2002) archetypes were applicable to warm season rainfall events as well. Our results showed that the AR events could be classified into three of the four Berger *et al.* (2002) types, with the exception of NW flow types. Most of the AR in Table 2 were classified as PR events, and our analysis indicated that a similar number of AR were SW and RD events to rain and snow events overall. Also, the general synoptic configuration was similar to the results of the studies of Dirmeyer and Kinter III (2009; 2010) and Nakamura *et al.* (2013) for the Maya Express, that is, the presence of a long narrow corridor of moisture on the westwards side of the Bermuda High over the Southeast United States coast. Additionally, an examination of the synoptic configuration showed that all of our events could be classified as Western Gulf AR as defined by Debbage *et al.* (2017).

Lastly, although the sample size is small, the ENSO variability of AR occurrence was similar to the results of Guan and Waliser (2015), who suggested that there were more La

Niña AR in the central USA over the period 1997–2014. Additionally, the inter-annual variability (ENSO) of the synoptic regime showed similarities to previous longer-term climatological studies of snowfall or dew point in this region (e.g., Berger *et al.*, 2002; Lupo *et al.*, 2012; Newberry *et al.*, 2016). There was some variation with respect to the location and orientation of the IVT axis as well as the main surface and 850 hPa level synoptic features. However, all of these AR events exhibited a warm moist air advection signature, which implies vertical ascent and a baroclinic environment. Additionally, all the events were supported by upper-air divergence associated with jet maxima, and most of these cases showed the study region under the equatorwards entrance region of a jet located polewards and east of the region.

The findings from the CIMSS MIMIC-TPW and the HYSPLIT model indicated that the mid-Mississippi Valley heavier rainfall events occurred in association with air masses originating from the tropics confirming the results of many studies cited in this work. Furthermore, when the air parcels traversed closer to the surface of the ocean during the 48 hr preceding the day of the event, there was increased heavy rainfall potential. When those parameters were coupled with upper-air soundings, which had vertically veering wind profiles, there was a greater propensity for the generation of atmospheric environments even more conducive for heavy rainfall events. Lastly, there was a tendency for frontal boundaries and/or synoptic-scale systems with a perpendicular orientation with respect to the AR (i.e., often a slow-moving west-to-east oriented warm or stationary front) to produce substantially less rainfall than those features with a parallel orientation in the study region (e.g., a faster-moving south-to-north oriented cold front). In forecasting for future heavy rainfall events, these results demonstrate that thorough analysis of both air mass behaviour and upper-air soundings would lend useful insights for generating improved forecasts.

The findings from different components of the upper-air sounding analysis reinforced the importance of utilizing upper-air data in operational forecasting. Over the last few years, there has been an increase in the number of discussions focused on evaluating how atmospheric research can better utilize financial and logistic resources for future upper-air observation platforms. Future upper-air research should continue developing modernized approaches for studying global atmospheric profiles. To move forwards, atmospheric research will continue the current trajectory towards maximizing the utilization of geostationary orbiting satellites (e.g., implementation of GOES-16 and GOES-17) to conduct such measurements.

ACKNOWLEDGEMENTS

The authors would like to thank the two anonymous reviewers for their time and effort in helping to make this

contribution stronger. This work was partially funded by USDA Research Support Agreement Nos. 58-3622-4-025 and 58-5070-5-018 under “Rainfall Rates in North-Central Missouri’s LTAR.”

CONFLICT OF INTEREST

The authors declare no potential conflict of interests.

REFERENCES

- Air Resources Laboratory (ARL). (2017) *HYSPLIT model*. Maryland: Air Resources Laboratory NCWCP, R/ARL. <http://www.arl.noaa.gov/hysplit/hysplit/> [Accessed 21th March 2019].
- Alishouse, J.C., Snyder, S., Vongsathorn, J. and Ferraro, R. (1990) Determination of total precipitable water from the SSM/I. *IEEE Transactions on Geoscience and Remote Sensing*, 28, 811–816.
- American Meteorological Society. (2017) *Glossary of Meteorology*. Boston, MA: American Meteorological Society. Available at: http://glossary.ametsoc.org/wiki/Atmospheric_river. [Accessed 7th February 2019].
- Berger, C.L., Lupo, A.R., Browning, P., Bodner, M., Chambers, M.D. and Rayburn, C.C. (2002) A climatology of northwest Missouri snowfall events: long-term trends and interannual variability. *Physical Geography*, 23(6), 427–448.
- Bluestein, H.B. and Banacos, P.C. (2001) The vertical profile of wind and temperature in cyclones and anticyclones over the eastern two-thirds of the United States: a climatology. *Monthly Weather Review*, 130, 487–505.
- Bosart, L.F., Moore, B.J., Cordeira, J.M. and Archambault, H.M. (2017) Interactions of North Pacific tropical, midlatitude, and polar disturbances resulting in linked extreme weather events over North America in October 2007. *Monthly Weather Review*, 146, 1245–1273.
- Center for Ocean and Atmosphere Prediction Studies (COAPS). (2017) *Resources and outreach*. Available at: <http://www.coaps.fsu.edu> [Accessed 19th May 2017].
- Cooperative Institute for Meteorological Satellite Studies (CIMSS). (2017) *Morphed Integrated Microwave Imagery at CIMSS Total Precipitable Water (MIMIC-TPW)*. Madison, WI : University of Wisconsin - Madison Space Science and Engineering Center. Available at: <http://tropic.ssec.wisc.edu/real-time/mimic-tpw/natl/main.html> [Accessed 19th May 2017].
- Debbage, N., Miller, P., Poore, S., Morano, K., Mote, T. and Sheppard, J.M. (2017) A climatology of atmospheric river interactions with the southeastern United States coastline. *International Journal of Climatology*, 37, 4077–4091.
- Dettinger, M., Ralph, M., Das, T., Neiman, P. and Cayan, D. (2011) Atmospheric rivers, floods and the water resources of California. *Water*, 3(2), 445–478.
- Dirmeyer, P.A. and Kinter, J.L., III. (2009) The “Maya Express”: floods in the U.S. Midwest. *Eos, Transactions American Geophysical Union*, 90, 101–102.
- Dirmeyer, P.A. and Kinter, J.L., III. (2010) Floods over the U.S. Midwest: a regional water cycle perspective. *Journal of Hydrometeorology*, 11, 1174–1180.
- Donohoe, A., Marshall, J., Ferreira, D. and McGee, D. (2013) The relationship between ITCZ location and cross-equatorial atmospheric heat transport: from the seasonal cycle to the last glacial maximum. *Journal of Climate*, 26, 3597–3617.
- Guan, B. and Waliser, D.E. (2015) Detection of atmospheric rivers: evaluation and application of an algorithm for global studies. *Journal of Geophysical Research: Atmospheres*, 120, 12514–12545. <https://doi.org/10.1002/2015JD024257>.
- Hastenrath, S. (1966) The flux of atmospheric water vapour over the Caribbean Sea and the Gulf of Mexico. *Journal of Applied Meteorology*, 5, 778–788.
- Higgins, R.W., Kousky, V.E. and Xie, P. (2011) Extreme precipitation events in the south-central United States during May and June 2010: historical perspective, role of ENSO, and trends. *Journal of Hydrometeorology*, 12, 1056–1070.
- Hirschboeck, K.K. (1991) Hydrology of floods and droughts: climates and floods. *National Water Summary*, 2(375), 67–88.
- Junker, N.W., Schneider, R.S. and Fauver, S.L. (1999) A study of heavy rainfall events during the Great Midwest Flood of 1993. *Weather and Forecasting*, 14, 701–712.
- Kalnay, E., Kanamitsu, M., Kistler, R., et al. (1996) The NCEP/NCAR 40-year reanalysis project. *Bulletin of the American Meteorological Society*, 77, 437–471.
- Kastman, J.S., Market, P.S., Fox, N.I., Foscatto, A.L. and Lupo, A.R. (2017b) Lightning and rainfall characteristics in elevated versus surface based convection in the Midwest that produce heavy rainfall. *Atmosphere*, 8, 36.
- Kastman, J.S., Market, P.S., Rochette, S.M. and Lupo, A.R. (2017a) Assessing upper tropospheric jet streak proximity using the Rossby radius of deformation. *Atmosphere*, 8, 2. <https://doi.org/10.3390/atmos8010002>.
- Knippertz, P., Wernli, H. and Gläser, G. (2013) A global climatology of tropical moisture exports. *Journal of Climate*, 26, 31–32.
- Lavers, D.A. and Villarini, G. (2013) Atmospheric rivers and flooding over the central United States. *Journal of Climate*, 26(7), 829–836.
- Lupo, A.R., Li, Y.C., Feng, Z.C., Fox, N.I., Rabinowitz, J.L. and Simpson, M.A. (2016) Sensitive versus rough dependence on initial conditions in atmospheric flow regimes. *Atmosphere*, 7, 157. <https://doi.org/10.3390/atmos7120157>.
- Lupo, A.R., Smith, N.B., Guinan, P.E. and Chesser, M.D. (2012) The climatology of Missouri Region dew points and the relationship to ENSO. *National Weather Digest*, 36, 81–91.
- Lupo, A.R. and Smith, P.J. (1995) Climatological features of blocking anticyclones in the Northern Hemisphere. *Tellus A*, 47(4), 439–456.
- Mahoney, K., Jackson, D.L., Neiman, P., Hughes, M., Darby, L., Wick, G., White, A., Sukovich, E. and Cifelli, R. (2016) Understanding the role of atmospheric rivers in heavy precipitation in the Southeast United States. *Monthly Weather Review*, 144, 1617–1632. <https://doi.org/10.1175/MWR-D-15-0279.1>.
- Mayer, M., Haimberger, L. and Balmaseda, M.A. (2014) On the energy exchange between tropical ocean basins related to ENSO. *Journal of Climate*, 27, 6393–6403.
- Messinger, F., DiMego, G., Kalnay, E., Mitchell, K., Shafran, P.C., Ebisuzaki, W., Jovic, D., Woollen, J., Rogers, E., Berbery, E.H., Ek, M.B., Fan, Y., Grumbine, R., Higgins, W., Li, H., Lin, Y., Manikin, G., Parrish, D. and Shi, W. (2006) North American regional reanalysis. *Bulletin of the American Meteorological Society*, 87, 343–360.
- Miller, D.K., Hotz, D., Winton, J. and Stewart, L. (2018) Investigation of atmospheric rivers impacting the Pigeon River basin of the southern Appalachian Mountains. *Weather and Forecasting*, 33, 283–299. <https://doi.org/10.1175/WAF-D-17-0060.1>.
- Molinari, J. (1986) Air mass modification over the eastern Gulf of Mexico as a function of surface wind fields and Loop Current position. *Monthly Weather Review*, 115, 646–652.
- Moore, B.J., Neiman, P.J., Ralph, F.M. and Barthold, F.E. (2012) Physical processes associated with heavy flooding rainfall in Nashville, Tennessee, and vicinity during 1–2 May 2010: the role of an atmospheric river and mesoscale convective systems. *Monthly Weather Review*, 140, 358–378.
- Nakamura, J., Lall, U., Kushnir, Y., Robertson, A.W. and Seager, R. (2013) Dynamical structure of extreme floods in the U.S. Midwest and United Kingdom. *Journal of Hydrometeorology*, 14, 485–504. <https://doi.org/10.1175/JHM-D-12-059.1>.
- National Weather Service, St. Louis Office. (2017) *Climate and past weather*. Available at: http://w2.weather.gov/climate/local_data.php?wfo=lsx [Accessed 19th May 2017].
- Neiman, P.J., Ralph, F.M., Wick, G.A., Lundquist, J.D. and Dettinger, M.D. (2008) Meteorological characteristics and overland precipitation aspects of atmospheric rivers affecting the west coast of North America based on eight years of SSM/I satellite observations. *Journal of Hydrometeorology*, 9, 22–47.
- Newberry, R.G., Lupo, A.R., Jensen, A.D. and Rodrigues-Zalipynis, R.A. (2016) An analysis of the spring-to-summer transition in the west central plains for application to long range forecasting. *Atmospheric and Climate Sciences*, 6, 375–393.
- Newell, R.E., Newell, N.E., Zhu, Y. and Scott, C. (1992) Tropospheric rivers?: a pilot study. *Geophysical Research Letters*, 19, 2401–2404. <https://doi.org/10.1029/92GL0216>.
- NOAA Storm Prediction Center. (2017) *Storm reports*. Available at: <http://www.spc.noaa.gov/expert/archive/events/> [Accessed 19th May 2017].

- Plymouth State University Weather Center. (2017) *Upper air*. Available at: <http://vortex.plymouth.edu/uacalplt-u.html> [Accessed 19th May 2017].
- Sanders, F. and Gyakum, J.R. (1980) Synoptic–dynamic climatology of the “bomb”. *Monthly Weather Review*, 108, 1577–1589.
- Schneider, R.S., Dean, A.R., Weiss, S.J., and Bothwell, P.D. (2006) Analysis of estimated environments for 2004 and 2005 severe convective storm reports. *Preprints, 23rd Conf. Severe Local Storms*. St. Louis MO: American Meteorological Society (AMS).
- Stein, A.F., Draxler, R.R., Rolph, G.D., Stunder, B.J.B., Cohen, M.D. and Ngan, F. (2015) NOAA’s HYSPLIT atmospheric transport and dispersion modeling system. *Bulletin of the American Meteorological Society*, 96, 2059–2077. <https://doi.org/10.1175/BAMS-D-14-00110.1>.
- Steinschneider, S. and Lall, U. (2015) A hierarchical Bayesian regional model of nonstationary precipitation extremes in Northern California conditioned on tropical moisture exports. *Water Resources Research*, 51(3), 1472–1492.
- Stephens, G.L. and Kummerow, C.D. (2006) The remote sensing of clouds and precipitation from space: a review. *Journal of the Atmospheric Sciences*, 64, 3742–3765.
- Stunder, B.J.B., Heffter, J.L. and Draxler, R.R. (2007) Airborne volcanic ash forecast area reliability. *Weather and Forecasting*, 22, 1132–1139. <https://doi.org/10.1175/WAF1042.1>.
- Thiao, W., Scofield, R.A. and Robinson, J. (1995) The relationship between water vapour plumes and extreme rainfall events during the summer season. *National Weather Digest*, 19, 26–49.
- Thieken, A.H., Kreibich, H., Muller, M. and Merz, B. (2010) Coping with floods: preparedness, response and recovery of flood-affected residents in Germany in 2002. *Hydrological Sciences Journal*, 52, 1016–1037.
- University of Wyoming Weather. (2017) *Upper air observations*. Available at: <http://weather.uwyo.edu/upperair/sounding.html> [Accessed 19th May 2017].
- Wang, S. and Chen, T. (2009) The late-spring maximum of rainfall over the U.S. Central Plains and the role of the low-level jet. *Journal of Climate*, 22, 4696–4698, 4707–4708.
- Wentz, F.J., Hilburn, K.A. and Smith, D.K. (2017) *Remote sensing systems DMSP [SSM/I or SSMIS] [daily, 3-day, weekly, monthly] environmental suite on 0.25 deg grid, version 7*. Santa Rosa, CA: Remote Sensing Systems. Available at: <http://www.remss.com/missions/ssmi> [Accessed 1st May 2017].

How to cite this article: Rabinowitz JL, Lupo AR, Market PS, Guinan PE. An investigation of atmospheric rivers impacting heavy rainfall events in the North-Central Mississippi River Valley. *Int J Climatol.* 2019;1–16. <https://doi.org/10.1002/joc.6061>